

Robust Control Design for Flexible Guidance of the Aerodynamic Descent of Reusable Launchers

Andrea Iannelli ^{*},
University of Stuttgart, Stuttgart 70569, Germany

Dimitris Gkouletsos [†], Roy S. Smith [‡]
Swiss Federal Institute of Technology, ETH Zürich, Zürich 8092, Switzerland

Rocket reusability is a key-factor for a sustainable and cost-effective future of space missions. Despite successes in this technology, some of the open problems remain an impediment to further development. For example, the descent phase presents important challenges from a guidance and control perspective, because, due to model and environment uncertainty, the optimal re-entry trajectory is often unknown *a priori*. As a result, the previously designed (or *offline*) controller may be unable to track the reference trajectories provided by the adaptive (or *online*) guidance algorithm. This paper is an attempt to build up a methodology to address this issue. First, a systematic approach for \mathcal{H}_∞ control design for a pre-defined nominal descent trajectory is described. The synthesis approach combines a disturbance rejection structured \mathcal{H}_∞ design at fixed operating conditions with a blended gain-scheduling approach across different altitudes. Then, the problem of providing robustness over a family of reference trajectories is framed as a multi-plant control design approach. The proposed robust control synthesis approach shows a satisfactory performance with respect to system requirements in the face of a large variation in the tracked trajectories and provides a novel viewpoint on designing robust controllers to successfully deploy flexible guidance algorithms.

I. Introduction

THE concept of rocket reusability has become central in space applications, owing to its prospect of markedly reducing manufacturing and mission costs. Commercial space companies have already successfully landed space vehicles to Earth in numerous flight tests [1]. However, there are still some standing problems which require further understanding. These can be exemplified by considering a typical launch and recovery mission profile for a notional two-stage launcher (Figure 1). Initially, the main engine is activated and the vehicle starts a vertical lift-off. During the powered ascent phase, the vehicle begins a pitch maneuver to follow a pre-programmed trajectory. At a pre-defined point, the vehicle's main engine cuts off and stage separation occurs. After separation, the second stage ignites its own engine and continues its journey towards space. Meanwhile, the first stage travels towards the recovery pad with a high horizontal velocity and a gradually increasing vertical velocity due to gravity. Cold-gas thrusters and fins are activated and control the first stage to prepare it for landing. During the descent flight, the fins become the primary actuators as their effectiveness gradually grows due to increasing air density. As the vehicle comes closer to the ground, the first stage main engine is reignited for the landing burn phase to accomplish a vertical landing on the recovery pad.

^{*}Assistant Professor, Institute for Systems Theory and Automatic Control, University of Stuttgart, Germany (andrea.iannelli@ist.uni-stuttgart.de)

[†]M.Sc. Graduate student, ETH Zürich, Switzerland

[‡]Professor, Automatic Control Lab, ETH Zürich, Switzerland, Associate Fellow AIAA

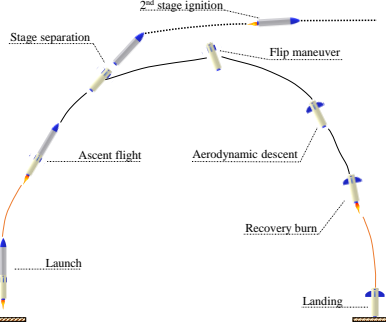


Fig. 1 Ascent and descent phases of a reusable launch vehicle.

Most of the technical challenges faced nowadays lie in the descent and reentry phases, mainly due to the fact that: aerodynamic fins and cold thrusters, the only actuators available for most of the mission after stage separation, have limited effectiveness, which strongly depend on the fast-varying atmospheric conditions; the main engine can only reignite below a specific altitude due to low fuel resources; an accurate vertical pinpoint landing with low velocities is required; and there is a high uncertainty associated with the environment and the operating conditions. For these reasons, a successful descent flight can only be achieved through a careful design of the guidance and control (G&C) algorithms, where the former provides the trajectory references to bring the vehicle onto the landing pad, and the latter is responsible for generating the actions required to follow the prescribed trajectory. Due to the aforementioned uncertainty, the optimal trajectory is not known exactly in the design stage, and is instead optimized in real-time by the online guidance algorithm. This flexible guidance gives rise to a family of possible references that the controller should be able to track, creating a type of robustness requirement that is less compelling in other applications.

Controller design has traditionally been a key enabler for successful rocket launches, as apparent by the rich literature on ascent atmospheric flight missions. A classic Proportional-Integral-Derivative (PID) scheme was used for attitude stabilization of decoupled pitch and yaw axes during the Saturn V launch mission [2]. Its successes enabled future projects such as the Space Shuttle [3] and Ares I, where the control system included bending filters for compensation of flexible modes [4]. Owing to the limitations of PID when addressing multivariable problems, Linear Quadratic Gaussian control was also considered [5], but without making a strong impact owing to its lack of robustness with respect to parametric uncertainty and limited disturbance rejection capability [6]. These drawbacks motivated the adoption of more sophisticated designs such as \mathcal{H}_∞ robust control [7]. Of particular relevance to this work are earlier studies that leveraged robust control techniques to track a variety of trajectories without requiring significant redesign of the controller [8], and the structured \mathcal{H}_∞ framework [9], which has already attracted much attention in launcher applications [10, 11]. In addition to the disturbance rejection properties achieved by design with \mathcal{H}_∞ control, the structured version allows the designer to assign a specified structure to the controller. This often allows lower order controllers with higher interpretability of the individual components to be obtained. Moreover, these controllers are generally better suited for gain-scheduling as they can be designed in different operating points but with similar properties, thus making their interpolation more reliable. Works on the descent and landing phases are only recently emerging. The study in [12] gives an holistic viewpoint considering flight mechanics, control and guidance aspects during descent flight. From a control perspective, only the pitch channel is addressed through the design of an adaptive PD controller. In [13] structured \mathcal{H}_∞ is used for control of the aerodynamic descent phase. The authors consider decoupled attitude and translational channels and design independent controllers for each control axis. Robust control compensators for descent and landing on small planetary bodies was addressed in [14] by adopting translational vehicle dynamics and providing a systematic approach for handling uncertainties with structured \mathcal{H}_∞ synthesis.

It is clear that whereas the design of the ascent phase can benefit from the rich G&C literature developed for conventional (non-reusable) launchers, works devoted to the aforementioned specific issues of the descent and reentry phases are scarce. This paper investigates the problem of robust controller design for the descent phase of reusable launch vehicles (RLVs) and gives a twofold contribution to the literature: first, a systematic structured \mathcal{H}_∞ and gain scheduling synthesis procedure tailored to the descent phase is illustrated; second, a novel design that gives robustness against the variability of the reference trajectories generated by the guidance algorithm is proposed. More precisely, we consider the aerodynamic descent phase of a notional RLV, which in accordance with the state-of-the-art mission analysis (e.g. see the CALLISTO project analyzed in [15]) dominates the descent phase as the main engine reignites only for landing in the last 2-3 kilometers altitude. In this flight phase, the limited actuation power due to the availability

of only fins and cold thrusters imposes restrictions on the controllability of the system. Moreover, planning is critical owing to the uncertainty in the environment and the RLV after the flip maneuver. This makes the G&C problem very challenging.

The main contents of the paper are summarized as follows:

- Section II presents a fully-coupled translational and attitude system dynamics, unlike in the majority of prior work where decoupled pitch and yaw axes based on the assumption of low roll rates are considered.
- Section III formulates a robust control design for wind rejection leveraging structured \mathcal{H}_∞ synthesis at fixed points along a pre-defined nominal trajectory and input blending for gain scheduling. Careful consideration is paid to the descent phase specific aspects reviewed earlier.
- Section IV considers the problem of robustifying the controller against a family of reference trajectories, instead of a single nominal one as typically done. This is a first step towards employing offline controllers that can cope with a range of trajectories prescribed during flight by the online guidance algorithm.
- Section V presents an extensive analysis to assess prospective advantages of the proposed controllers.

II. Control-oriented modeling of the aerodynamic descent phase

This Section describes the first-principles modeling approach adopted to model the RLV system, which follows to a large extent the procedure presented in [12] for a vehicle model inspired by the VEGA launcher. The RLV properties are also defined based on the values reported therein. The model developed here has a twofold goal: its linearization about pre-defined trajectories is used for control design; and the associated nonlinear simulator is used for the assessment of the controllers through time-domain analyses.

A. Reference frames

The motion of an RLV during the descent flight mission can be described by making use of the following reference frames [16]: Earth-centered inertial frame (ECI); Earth-centered, Earth-fixed frame (ECEF); Launch pad frame (LP); and Body frame (B). The ECI frame's origin coincides with the Earth center, the X_I axis points towards the vernal equinox, the Z_I axis points towards the north pole and the Y_I axis lies on the celestial equator. The orthonormal basis of ECI along the axes (X_I, Y_I, Z_I) is denoted by $(_I i, _I j, _I k)$. Based on the assumption that Earth's motion around the sun is negligible for reentry space applications, the ECI frame is considered inertial and, thus, can be used for the equations of motion. The position and velocity vectors of the launch vehicle in ECI frame will be denoted by $_I r$ and $_I v$.

Similarly to ECI, the ECEF frame's origin coincides with the Earth center, the Z_E axis points towards the north pole, while the X_E and Y_E axes lie on the celestial equator plane with the X_E axis pointing towards the prime meridian. The ECEF orthonormal basis is denoted by $(_E i, _E j, _E k)$. The ECEF frame rotates around the ECI frame with the Earth's angular velocity $_I \Omega = \Omega_I k = \Omega_E k$. To describe the orientation from ECI to ECEF frame, the time-varying rotation matrix C_{EI} is used

$$C_{EI}(t) = \begin{bmatrix} \cos \Omega t & \sin \Omega t & 0 \\ -\sin \Omega t & \cos \Omega t & 0 \\ 0 & 0 & 1 \end{bmatrix} C_{EI}(0).$$

The LP frame is assumed here to be located at the European Space Centre in French Guiana [17] with origin in geodetic coordinates $(\varphi_{\text{launch}}, \lambda_{\text{launch}}, h_{\text{launch}}) \approx (5.2^\circ, -52.8^\circ, 0\text{m})$. The Y_L and Z_L axes point towards east and the north pole, respectively, while the X_L axis points upwards and vertically to the local earth plane. The LP frame is fixed with respect to ECEF, but with a different orientation expressed by the rotation matrix

$$C_{EL} = \begin{bmatrix} \cos \varphi_{\text{launch}} \cos \lambda_{\text{launch}} & -\sin \lambda_{\text{launch}} & -\sin \varphi_{\text{launch}} \cos \lambda_{\text{launch}} \\ \cos \varphi_{\text{launch}} \sin \lambda_{\text{launch}} & \cos \lambda_{\text{launch}} & -\sin \varphi_{\text{launch}} \sin \lambda_{\text{launch}} \\ \sin \varphi_{\text{launch}} & 0 & \cos \varphi_{\text{launch}} \end{bmatrix}.$$

It is convenient to express kinematics in the LP frame using the formulas

$$\begin{aligned} Lr &= C_{LE} C_{EI} (_I r - _I r_{\text{launch}}), \\ Lv &= C_{LE} C_{EI} (_I v - _I \Omega \times_I r), \end{aligned}$$

where $_I r_{\text{launch}}$ is the launch position vector in ECI, Lr and Lv are the position and velocity vectors, respectively, in the LP frame.

The origin of the body frame B is set to the center of gravity (CG). Note that since, as discussed later, in the unpowered descent phase the mass is assumed constant, this point does not change in time. The longitudinal distance of CG from the launcher base will be denoted by x_{CG} . The axis X_B points towards the vehicle's longitudinal axis, Y_B is orthogonal to the pitch plane and Z_B completes the right-handed system. The B frame orthonormal basis is denoted by $(_B i, _B j, _B k)$.

To describe vehicle's orientation with respect to ECI, the unit-norm quaternion $q_{IB} = (q_0, q_1, q_2, q_3)$ is used where q_0 is the scalar part and (q_1, q_2, q_3) is the imaginary vector part. Quaternions are a convenient way of describing angular quantities and are extensively used in space applications [18, 19]. Unit-norm quaternions define a rigid body orientation via a rotation around an axis $e_{rot} \in \mathbb{R}^3$ and an angle θ_{rot} . The scalar part can then be defined as $q_0 = \cos(\theta_{rot}/2)$ and the vector part as $(q_1, q_2, q_3) = e_{rot} \sin(\theta_{rot}/2)$. Unit-norm quaternions provide a non-minimal representation of rotation since they satisfy the relationship $q_0^2 + q_1^2 + q_2^2 + q_3^2 = 1$. Quaternions present advantages compared to Euler angles since they avoid geometrical singularities and are computationally faster due to the use of product relations instead of trigonometrical functions [20]. A quaternion q_{IB} corresponds to the rotation matrix

$$C_{IB} = \begin{bmatrix} 1 - 2(q_2^2 + q_3^2) & 2(q_1q_2 - q_0q_3) & 2(q_0q_2 + q_1q_3) \\ 2(q_1q_2 + q_0q_3) & 1 - 2(q_1^2 + q_3^2) & 2(q_2q_3 - q_0q_1) \\ 2(q_1q_3 - q_0q_2) & 2(q_0q_1 + q_2q_3) & 1 - 2(q_1^2 + q_2^2) \end{bmatrix}.$$

B. Equations of Motion

The equations of motion for a notional RLV are presented here. Since the focus is on the aerodynamic descent phase, actuation takes place through: aerodynamic fins, which leverage higher aerodynamic forces as altitude decreases due to higher density; and cold gas thrusters. During the unpowered descent phase the mass and moment of inertia derivatives are negligible. The vehicle center of gravity CG is located on the body frame longitudinal axis and is defined by $_B r_{CG} = [x_{CG} \ 0 \ 0]^\top$, where x_{CG} , due to the assumption on the mass variation, is constant.

The translational equations of motion in ECI frame are

$${}_I \ddot{r} = {}_I \dot{v} = {}_I g + \frac{1}{m} ({}_I F_{\text{thr}} + {}_I F_{\text{aero}} + {}_I F_{\text{fins}}), \quad (1)$$

where g is the gravitational acceleration, F_{thr} the cold-gas thrusters force, F_{aero} the aerodynamic force and F_{fins} the fins force. Translational quantities are then expressed in the LP frame in terms of altitude (x-direction), crossrange (y-direction) and downrange (z-direction). This introduces fictitious forces such as the Coriolis and the centripetal accelerations

$${}_L \dot{v} = C_{LI} {}_I g + C_{LI} \frac{1}{m} ({}_I F_{\text{thr}} + {}_I F_{\text{aero}} + {}_I F_{\text{fins}}) - 2 {}_L \Omega \times {}_L v - {}_L \Omega \times ({}_L \Omega \times {}_L r). \quad (2)$$

The rotational dynamics with respect to the B frame are

$${}_B \dot{\omega} = J^{-1} ({}_B M_{\text{thr}} + {}_B M_{\text{aero}} + {}_B M_{\text{fins}} - {}_B \omega \times (J {}_B \omega)), \quad (3)$$

where ${}_B \omega$ is the angular velocity of the vehicle with respect to ECI, J is the moment of inertia tensor expressed in the B frame passing through the vehicle's center of mass and ${}_B M$ are moments produced by the forces in (1). Rotational dynamics and orientation are connected via the following relationship between angular velocity and quaternion [18]

$$\dot{q}_{IB} = \frac{1}{2} G (q_{IB})_B \omega, \quad G = \begin{bmatrix} -q_1 & -q_2 & -q_3 \\ q_0 & -q_3 & q_2 \\ q_3 & q_0 & -q_1 \\ -q_2 & q_1 & q_0 \end{bmatrix}. \quad (4)$$

Equations (1)-(4) describe the dynamics of the vehicle. Forces and moments featuring these equations are discussed in more detail next.

1. Aerodynamics and atmospheric models

The generation of aerodynamic loads is mainly a function of the geometrical characteristics of the vehicle and the dynamic pressure Q , given by $Q = \frac{1}{2}\rho \|_B v_{\text{air}}\|_2^2$, where ρ is the air density and $_B v_{\text{air}}$ is the vehicle's velocity relative to the Earth's motion and wind velocity $_B v_{\text{wind}}$

$$_B v_{\text{air}} = _B v - C_{BI} I \Omega \times I r - _B v_{\text{wind}}, \quad (5)$$

Next, define the angle of attack, $\alpha = \arctan_2 \left(\frac{B v_{\text{air},z}}{B v_{\text{air},x}} \right)$, as the angle between vehicle's longitudinal axis and airspeed projection to body XZ plane, and define the sideslip, $\beta = \arcsin \left(\frac{B v_{\text{air},y}}{\|B v_{\text{air}}\|_2} \right)$, as the angle between airspeed and body XZ plane [21]. The resulting so-called *effective* angle of attack is

$$\alpha_{\text{eff}} = \arccos(\cos \alpha \cos \beta) \approx \sqrt{\alpha^2 + \beta^2}. \quad (6)$$

The air-relative velocity (ARV) reference frame is convenient to characterize the aerodynamic loads. It has its origin fixed to the vehicle's center of mass and X_V axis pointing to the direction of airspeed velocity v_{air} . The axes Y_V and Z_V are defined with respect to the angle of attack and sideslip, as shown in Figure 2. The rotation matrix from B frame to ARV frame is computed as

$$C_{VB} = \begin{bmatrix} \cos \alpha \cos \beta & \sin \beta & \sin \alpha \cos \beta \\ -\sin \beta \cos \alpha & \cos \beta & -\sin \alpha \sin \beta \\ -\sin \alpha & 0 & \cos \alpha \end{bmatrix}.$$

The aerodynamic force is depicted in Figure 3 and can be expressed in ARV as

$$_V F_{\text{aero}} = -QS_{\text{aero}} \begin{bmatrix} C_D \\ 0 \\ C_L \end{bmatrix}, \quad (7)$$

where S_{aero} is the aerodynamic reference surface corresponding to the cross-section of the RLV, C_D and C_L are the drag and lift coefficients, respectively. Aerodynamic forces are applied on the center of pressure, which lies on the vehicle's longitudinal axis at a distance x_{CP} from the launcher base. Transforming the aerodynamic force into the B frame can be done by applying $_B F_{\text{aero}} = C_{VB}^T V F_{\text{aero}}$. The corresponding aerodynamic moments are derived based on

$$_B M_{\text{aero}} = _B r_{CG \rightarrow CP} \times _B F_{\text{aero}}, \quad _B r_{CG \rightarrow CP} = \begin{bmatrix} (x_{CP} - x_{CG}) & 0 & 0 \end{bmatrix}^T. \quad (8)$$

The drag C_D and lift C_L coefficients and the vehicle's center of pressure position x_{CP} , taken from [12], are a function of α_{eff} and the Mach number.

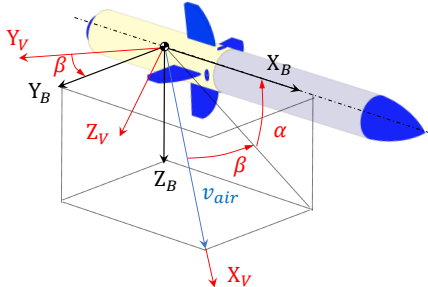


Fig. 2 ARV frame.

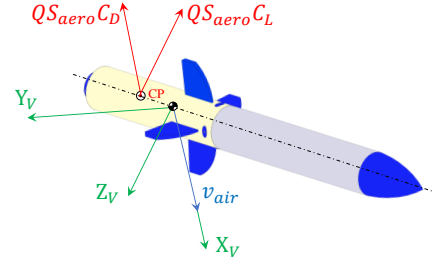


Fig. 3 Aerodynamic forces.

The gravity term $I g$ in (1) is calculated according to

$$I g = C_{IE} E g_{\text{egm}} (Er),$$

where g_{egm} is the spherical harmonic representation of gravity based on the EGM2008 planetary model [22] and $Er = C_{EI} I r$. The air density ρ and speed of sound are calculated as a functions of the altitude based on the atmospheric model 1976 COESA [23].

2. Actuators: fins and cold thrusters

Fins are used to produce aerodynamic control forces and moments in the presence of a non-negligible dynamic pressure Q . Following [12], two pairs of fins symmetrically located around the vehicle's longitudinal axis are considered. The first pair is perpendicular to the $B\ XZ$ plane (pitch plane) with fins deflection angles $\delta_{\text{fin},1}$ and $\delta_{\text{fin},2}$, while the second pair is perpendicular to the $B\ XY$ plane (yaw plane) with angles $\delta_{\text{fin},3}$ and $\delta_{\text{fin},4}$. The axial fin forces are omitted as the fin surface is significantly smaller compared to vehicle's body and thus only the normal fin force with contribution $C_{\text{fin}}(\alpha_{\text{fin},i}) = \bar{C}_{\text{fin}} \sin(\alpha_{\text{fin},i})$ [12] where $\alpha_{\text{fin},i}$ is i -th fin local angle of attack, is accounted for. The first pair of fin forces is given by

$${}_B F_{\text{fin},i} = Q S_{\text{fin}} C_{\text{fin}} (\alpha_{\text{fin},i}) \begin{bmatrix} -\sin \delta_{\text{fin},i} & 0 & \cos \delta_{\text{fin},i} \end{bmatrix}^{\top}, \quad i = \{1, 2\}$$

where $\alpha_{\text{fin},i} = \delta_{\text{fin},i} - \alpha$ and S_{fin} is the fin surface. Based on analysis for conventional airfoils [12], we set $\bar{C}_{\text{fin}} = 6$ and $S_{\text{fin}} = 0.54 \text{ m}^2$. The second pair is given by

$${}_B F_{\text{fin},i} = Q S_{\text{fin}} C_{\text{fin}} (\alpha_{\text{fin},i}) \begin{bmatrix} \sin \delta_{\text{fin},i} & \cos \delta_{\text{fin},i} & 0 \end{bmatrix}^{\top}, \quad i = \{3, 4\}$$

where $\alpha_{\text{fin},i} = -\delta_{\text{fin},i} - \beta$. We summarize fin forces into a single net force ${}_B F_{\text{fins}} = \sum_{i=1}^4 {}_B F_{\text{fin},i}$. The fin moments are given by

$${}_B M_{\text{fins}} = \sum_{i=1}^4 {}_B r_{CG \rightarrow \text{fin},i} \times {}_B F_{\text{fin},i},$$

where ${}_B r_{CG \rightarrow \text{fin},i} = [x_{\text{fin},i} - x_{CG} \quad 0 \quad 0]^{\top}$ and x_{fin} represents the longitudinal fin distance from the base.

Cold gas thrusters are used to provide additional actuation, especially at high altitudes where air density is low and, thus, aerodynamic fins have low effectiveness. The mass loss due to gas expansion is typically negligible, and their combined forces are

$${}_B F_{\text{thr}} = T_{\text{thr}} \begin{bmatrix} 0 \\ -\delta_{\text{thr},z} \\ \delta_{\text{thr},y} \end{bmatrix}, \quad (9)$$

where $T_{\text{thr}} = 1000 \text{ N}$ is the maximum force per thruster and $(\delta_{\text{thr},y}, \delta_{\text{thr},z})$ represent normalized commands for thrusters acting on the y and z direction, respectively, taking values in $[-1, 1]$. The corresponding thrusters moment is given by

$${}_B M_{\text{thr}} = T_{\text{thr}} \begin{bmatrix} 0 \\ -(x_{\text{thr},y} - x_{CG})\delta_{\text{thr},y} \\ -(x_{\text{thr},z} - x_{CG})\delta_{\text{thr},z} \end{bmatrix} + \begin{bmatrix} M_{\text{thr},x} \\ 0 \\ 0 \end{bmatrix}, \quad (10)$$

where $(x_{\text{thr},y}, x_{\text{thr},z})$ is the position of thrusters in the vehicle's longitudinal axis with respect to launcher's base. The first term of (10) represents the moments caused by ${}_B F_{\text{thr}}$. Because its line of action passes through the vehicle's longitudinal axis, it does not provide roll moment. To obtain control authority in the roll direction, the term $M_{\text{thr},x} = 2RT_{\text{thr}}\delta_{\text{thr},r}$ is added, where R is the radius of the vehicle's cross section and $\delta_{\text{thr},r}$ is an additional command defined in $[-1, 1]$. In particular, we assume that roll thrusters produce a force couple of magnitude $\delta_{\text{thr},r}$ tangentially to the vehicle's cross section resulting in a pure moment in a similar fashion to the Reaction Control System (RCS) in [24]. For the sake of simplicity, it is assumed $x_{fin} = x_{thr,y} = x_{thr,z} = x_{thr}$ [12].

3. Mass and inertia properties

In the aerodynamic phase the launcher consists of the dry first stage and the propellant (oxidizer and fuel), whose characteristic sizes are taken from [12]. The vehicle's mass is given by $m = m_{\text{prop}} + m_{\text{dry}}$, where m_{dry} is the dry first stage mass, $m_{\text{prop}} = m_{\text{fuel}} + m_{\text{oxid}}$ is the (constant) propellant mass during the unpowered descent phase, and m_{fuel} and m_{oxid} are fuel and oxidizer masses, respectively. The axis-symmetric shape assumption about the vehicle results in a diagonal inertia matrix $J = \text{diag}(J_x, J_y, J_z)$ with $J_y = J_z$. The interested reader is referred to [12, 25] for details on the parameters defining the inertial properties and their numerical values.

C. Nonlinear model and linearization

The set of ordinary differential equations describing the dynamics of the RLV are compactly summarized here. The equations capturing the translational (2), rotational (3) and orientation dynamics (4)

$$\begin{aligned} {}_L\dot{r} &= {}_L v, \\ {}_L\dot{v} &= C_{LI} {}_I g + C_{LB} \frac{1}{m} ({}_B F_{\text{thr}} + {}_B F_{\text{aero}} + {}_B F_{\text{fins}}) - 2 {}_L \Omega \times {}_L v - {}_L \Omega \times ({}_L \Omega \times {}_L r), \\ {}_B\dot{\omega} &= J^{-1} ({}_B M_{\text{thr}} + {}_B M_{\text{aero}} + {}_B M_{\text{fins}} - {}_B \omega \times (J {}_B \omega)), \\ \dot{q}_{IB} &= \frac{1}{2} G (q_{IB})_B \omega, \end{aligned} \quad (11)$$

can be rewritten as

$$\dot{x} = f(x, u, d), \quad (12)$$

where $x = [{}_L r^\top \quad {}_L v^\top \quad {}_B \omega^\top \quad q_{IB}^\top]^\top$ are the states, $u = [\delta_{\text{thr}}^\top \quad \delta_{\text{fins}}^\top]^\top$ are the control inputs with $\delta_{\text{thr}} = (\delta_{\text{thr},x}, \delta_{\text{thr},y}, \delta_{\text{thr},z})$, $\delta_{\text{fins}} = (\delta_{\text{fin},1}, \delta_{\text{fin},2}, \delta_{\text{fin},3}, \delta_{\text{fin},4})$ and $d = {}_L v_{\text{wind}}$ is the wind velocity disturbance. The measured output variables y are given by

$$y = [{}_L r_y \quad {}_L r_z \quad {}_L v^\top \quad {}_B \omega^\top \quad (q_{IB})_v^\top]^\top, \quad (13)$$

where $(q_{IB})_v$ is the imaginary vector part of the quaternion q_{IB} . This is because unit quaternions correspond to non-minimal representation of rotation and thus the imaginary part is sufficient to describe orientation. It is also worth mentioning that the quantity $(q_{IB})_{v,\text{ref}} - (q_{IB})_v$, typically used as feedback on the attitude error, is approximately equal to the vector part of the true quaternion error $q_{IB}^{-1} \times (q_{IB})_{\text{ref}}$, and this further motivates this choice of output.

In order to obtain linear models which can be used for control design, the nonlinear dynamics (12) is linearized by expanding f as a Taylor series around a generic operating point (x_0, u_0, d_0)

$$\dot{x} = f(x_0, u_0, d_0) + \frac{\partial f}{\partial x}|_{x_0, u_0, d_0}(x - x_0) + \frac{\partial f}{\partial u}|_{x_0, u_0, d_0}(u - u_0) + \frac{\partial f}{\partial d}|_{x_0, u_0, d_0}(d - d_0) + O(x, u, d). \quad (14)$$

Dropping the higher order terms and introducing the deviation vectors $\Delta x := x - x_0$, $\Delta u := u - u_0$ and $\Delta d := d - d_0$, one obtains the linear deviation dynamics

$$\dot{\Delta x} = A \Delta x + B \Delta u + B_d \Delta d, \quad (15)$$

where $A = \frac{\partial f}{\partial x}|_{x_0, u_0, d_0}$, $B = \frac{\partial f}{\partial u}|_{x_0, u_0, d_0}$ and $B_d = \frac{\partial f}{\partial d}|_{x_0, u_0, d_0}$. In a similar fashion, the deviation output Δy is given by

$$\Delta y = C \Delta x + D \Delta u + D_d \Delta d, \quad C = \begin{bmatrix} 0_{8 \times 1} & I_{8 \times 8} & 0_{8 \times 1} & 0_{8 \times 3} \\ 0_{3 \times 1} & 0_{3 \times 8} & 0_{3 \times 1} & I_{3 \times 3} \end{bmatrix}, \quad (16)$$

where D, D_d are zero matrices with appropriate dimensions. The matrices A, B , and B_d will be obtained with numerical linearization based on central differences.

D. Reference trajectory generation

The last step required before approaching the control synthesis problem is the definition of a desired reference trajectory for the descent phase, which is typically taken care of by the guidance algorithm.

Two main guidance strategies are typically considered [26]: open loop guidance, whereby the reference trajectory is computed offline and does not change during the descent mission; closed loop guidance, whereby the reference trajectory is generated online using real-time measurements from the vehicle to cope with disturbances and dynamic uncertainty and increase mission accuracy. Closed loop guidance is clearly more appealing, but is also more challenging from a control design perspective as the reference trajectory is unknown during the pre-flight control synthesis. Studying this behavior and proposing possible strategies to tackle the associated challenges is one of the goals of this work. First, the traditional *nominal* trajectory design is presented, followed by the definition of a family (or *tube*) of trajectories, which serves to emulate the closed loop guidance system behavior.

1. Nominal trajectory

The reference trajectory spans an altitude range from the beginning of descent mission (chosen here as 75 km) down to the Earth (≈ 0 km). Even though the aerodynamic descent terminates at the prespecified altitude (≈ 3 km for the CALLISTO project [15]) where the main engine is reignited, its length is extended here without loss of generality in order to investigate the capabilities of thrusters and fins at low altitudes where aerodynamic loads and wind gusts are strong.

The design of the nominal reference trajectory is decomposed in the translational and the attitude parts. The reference position and velocities of the translational part are derived using a ballistic profile. That is, the trajectory followed by the RLV starting from generic initial conditions under the effect of gravity and aerodynamic forces and no actuation.

In analogy to what was done in [12], attitude reference (i.e. quaternions and angular rates) are designed independently of the ballistic trajectory used for the translational part. Specifically, the reference quaternions are generated so that the vehicle obtains the desired angle of attack α_{ref} and sideslip angle β_{ref} . For the entire descent mission, we select $\beta_{\text{ref}} = 0^\circ$, while α_{ref} is driven smoothly through a first order filter $G_{\text{AoA}} = 1/(25s + 1)$ from its initial value towards 180° , motivated by the objective of keeping structural loads low (load relief control strategy).

The reference quaternions q_{ref} are computed using the following steps.

- 1) Given the current airspeed ${}_B v_{\text{air}}$ and the reference aerodynamic angles $(\alpha_{\text{ref}}, \beta_{\text{ref}})$, the reference airspeed $({}_B v_{\text{air}})_{\text{ref}}$ is computed. By using the constraint $\|{}_B v_{\text{air}}\|_2 = \|({}_B v_{\text{air}})_{\text{ref}}\|_2$ and Eq. (6), we have

$$\begin{aligned} ({}_B v_{\text{air},x})_{\text{ref}} &= -\|{}_B v_{\text{air}}\|_2 \sqrt{\frac{1 - \sin^2(\beta_{\text{ref}})}{1 + \tan^2(\alpha_{\text{ref}})}}, \\ ({}_B v_{\text{air},y})_{\text{ref}} &= \|{}_B v_{\text{air}}\|_2 \sin(\beta_{\text{ref}}), \\ ({}_B v_{\text{air},z})_{\text{ref}} &= \tan(\alpha_{\text{ref}}) ({}_B v_{\text{air},x})_{\text{ref}}. \end{aligned} \quad (17)$$

- 2) Next, the quaternion q_s representing the shortest rotation between $({}_B v_{\text{air}})_{\text{ref}}$ and ${}_B v_{\text{air}}$ is computed. This is given by

$$q_s = \left[\cos\left(\frac{q_{\text{angle}}}{2}\right) \quad \sin\left(\frac{q_{\text{angle}}}{2}\right) q_{\text{axis}} \right], \quad (18)$$

where q_{axis} and q_{angle} are

$$q_{\text{axis}} = \frac{({}_B v_{\text{air}})_{\text{ref}} \times {}_B v_{\text{air}}}{\|({}_B v_{\text{air}})_{\text{ref}} \times {}_B v_{\text{air}}\|_2}, \quad q_{\text{angle}} = \arctan_2\left(\frac{\|({}_B v_{\text{air}})_{\text{ref}} \times {}_B v_{\text{air}}\|_2}{({}_B v_{\text{air}})_{\text{ref}} \cdot {}_B v_{\text{air}}}\right). \quad (19)$$

- 3) Finally, the reference quaternion is obtained by multiplying the quaternion q_{IB} , representing the vehicle's current orientation, by q_s (\otimes represents quaternion product)

$$q_{\text{ref}} = q_{IB} \otimes q_s. \quad (20)$$

The reference angular rates ω_{ref} are obtained from

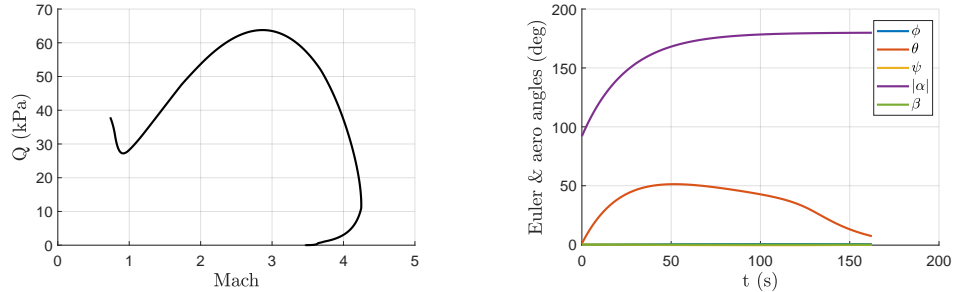
$$\begin{bmatrix} 0 \\ \omega_{\text{ref}} \end{bmatrix} = 2\dot{q}_{\text{ref}} \otimes q_{\text{ref}}^{-1}.$$

Figures 4a-4b illustrate the dynamic pressure and the reference aerodynamic and Euler angles profiles of the nominal trajectory, respectively. Whereas modelling and control are done here using quaternions, for visualization purposes we consider here and in Section V the roll-pitch-yaw (ϕ, θ, ψ) Euler angles with respect to launch pad frame.

2. Tube of trajectories

A simple idea to generate multiple reference trajectories consists of perturbing the initial conditions of the nominal one. Precisely, each trajectory is generated by selecting different lateral initial velocity components such that ${}_L v_y(t_0) \in [-200, 200]$ m/s and ${}_L v_z(t_0) \in [800, 1500]$ m/s where t_0 refers to the initial time condition. The trajectories are then computed using the same procedure outlined for the nominal case.

Table 1 shows the initial velocities for the perturbed trajectories, denoted by $RT_\#$, and Figure 5 illustrates the different perturbed trajectories together with the nominal one. In Figure 5a, we observe that the trajectories follow distinct



(a) Dynamic pressure (from Mach ≈ 3.5 at $t=0$ s to Mach ≈ 0.75 at $t=160$ s). (b) Euler and aero angles ((ϕ, ψ, β) featuring similar small values).

Fig. 4 Nominal reference trajectory.

profiles and land in different positions than the recovery pad as expected due to nature of the ballistic dynamics. Figure 5b shows the evolution of dynamic pressure and quantitatively shows the different aerodynamic load that each trajectory will determine on the vehicle. Even though this is not shown here for space limitations, there are important differences in attitude across the trajectories, because different initial velocities will result in different airspeed profiles and therefore in different reference quaternions (recall the discussion in Section II.D). It is apparent that the tube of trajectories presents deviations in both translational and attitude references, with clear impact on the change of underlying linearized dynamical model. Whereas other options have been considered to generate off-nominal trajectories (e.g. perturbing density or aerodynamic coefficients), the results were qualitatively similar and thus we propose here this methodology as it allows gaining a better intuition of the nature of the perturbations.

Table 1 Initial velocity conditions for nominal and perturbed trajectories.

Trajectory name	Downrange velocity (m/s)	Crossrange velocity (m/s)
Nominal	1000	0
RT_1	875	-25
RT_2	950	50
RT_3	1050	-25
RT_4	1100	50
RT_5	1150	-75
RT_6	1200	100
RT_7	1250	-125
RT_8	1300	150

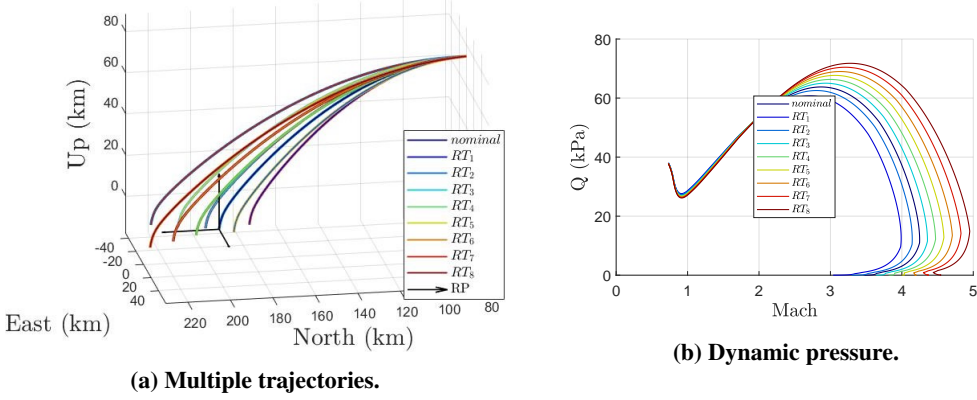


Fig. 5 Family of trajectories (tube) emulating the closed loop guidance.

III. Robust control design for nominal trajectory

This Section presents the first contribution of this paper, i.e. a methodology to design gain-scheduled structured \mathcal{H}_∞ controllers for the aerodynamic descent phase of a reusable launch vehicle along a fixed (nominal) reference trajectory. Section III.A defines the control objectives required for an RLV mission, while Section III.B describes the (structured) \mathcal{H}_∞ design and gain-scheduling approach proposed here. Section III.C finally defines the generalized plant and weights selections used for synthesis.

A. Controller Requirements

The high-level goal of an RLV controller is to satisfactorily follow the reference trajectory commanded by the guidance algorithm in order to successfully complete the descent flight mission. This objective can be articulated through a set of requirements which guide the controller synthesis:

- *Stability:*
The closed loop system should be stable, otherwise of course any other requirement can not be satisfied.
- *Attitude tracking:*
The system should track adequately attitude references such as quaternions and angular rates.
- *Position and velocity drifting:*
The controller should be able to reduce translational deviations from the reference trajectory. In terms of aerodynamic descent, this requirement is more loose due to the limited actuation.
- *Actuation limitation:*
Actuators should be used to an extent compatible with physical and technological limitations. For example, fins angles are able to deflect up to a certain amount of degrees.
- *Disturbance rejection:*
The control system should cope with external disturbances. The most common one is due to wind gusts which affect the aerodynamic angles and thus can increase loads.

Table 2 provides a quantitative measure for the aforementioned requirements. Most of them are inspired by the VEGA mission specifications [27], consistently with the modelling part which followed [12]. Explicit requirements about attitude angles, fins and thrusters actuation have also been added. Load minimization is here implicitly targeted by requiring the system to follow the attitude reference profile described earlier.

B. Gain-scheduled structured \mathcal{H}_∞ control problem formulation

1. Structured \mathcal{H}_∞ design

The closed-loop requirements defined in the previous section prescribes a set of performance and robustness properties that can be challenging to achieve in a complex system such as an RLV. The \mathcal{H}_∞ control paradigm has proved itself a successful candidate in space applications [11, 13, 14, 28, 29], and will be considered here as backbone of the synthesis procedure.

Table 2 Performance requirements for the RLV descent phase.

Requirement	Notation	Bounds
Attitude performance	Angles (ϕ, θ, ψ)	<4°
Drift performance	Position (r_y, r_z) Velocity (v_x, v_y, v_z)	<500 m <15 m/s
Actuation	Fins δ_{fin} Thruster δ_{thr}	<20° <1

The \mathcal{H}_∞ problem can be defined using the feedback interconnection depicted in Figure 6 where: P is the generalized plant and K is the controller; w and z represent exogenous disturbances and signals to be penalized, respectively (in the context of RLV, w could represent wind gusts while z the attitude and translational errors); e is the measured output and u is the controller output. Let us also denote by T_{wz} the closed loop transfer function given by the lower linear fractional transformation as $T_{wz} = \mathcal{F}_l(P, K)$ [30].

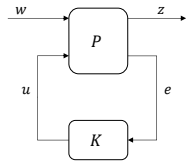


Fig. 6 H_∞ control interconnection.

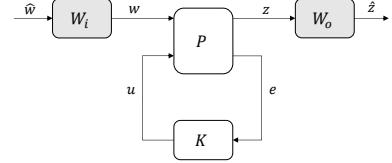


Fig. 7 Weighted H_∞ control interconnection.

The \mathcal{H}_∞ control problem objective is to find a stabilizing controller K such that the \mathcal{H}_∞ norm of T_{wz} is minimized

$$\begin{aligned} \min_K \|T_{wz}\|_\infty &= \min_K \max_\omega \bar{\sigma}(T_{wz}(j\omega)), \\ \text{s.t. } K \text{ stabilizes } P \text{ internally,} \end{aligned} \quad (21)$$

where $\bar{\sigma}$ denotes the maximum singular value operator.

Scaling of the optimization problem (21) is very important both to encode the desired system performance and numerically improve its solution [31]. Therefore, the baseline interconnection in Figure 6 is typically augmented by introducing input W_i and output W_o weights as shown in Figure 7. The new augmented closed loop transfer function \hat{T}_{wz} is given by $\hat{T}_{wz} = W_o T_{wz} W_i$. After appropriate weighting, a stabilizing controller K fulfilling the performance specifications will result in $\|\hat{T}_{wz}\|_\infty < 1$. The so-called generalized plant, comprising the weights and exogenous input w and output z , will be discussed in more detail in Section III.C.

The standard \mathcal{H}_∞ control problem (21) can be solved in different ways, e.g. by solving coupled Riccati equations [32] or with convex optimization programs based on linear matrix inequalities [33]. The resulting controller has at least the same order as the original plant, it typically does not offer intuition about the individual control components and might present implementation difficulties due to high-frequency poles. To ameliorate some of these issues an interesting strategy consists of imposing constraints on the controller structure, which lead to the concept of structured \mathcal{H}_∞ .

$$\begin{aligned} \min_K &\|W_o T_{wz} W_i\|_\infty, \\ \text{s.t. } K \text{ stabilizes } P \text{ internally,} \\ K \in \mathcal{K}_{\text{struct}}, \end{aligned} \quad (22)$$

where $\mathcal{K}_{\text{struct}}$ is the controller space defined by the imposed controller structure. Problem (22), unlike (21), is non-convex. In [9] the use of non-smooth optimization tools was proposed for its solution, and this approach is currently implemented in routines such as *hinstruct* or *systune* available with the Robust Control Toolbox from MATLAB®.

The set $\mathcal{K}_{\text{struct}}$ characterizing the structure enforced on the \mathcal{H}_∞ controller via program (22) is defined here starting from the following 7-order state space controller model

$$\left[\begin{array}{c} \dot{x}_K \\ u \end{array} \right] = \left[\begin{array}{c|c} A_K & B_K \\ \hline C_K & D_K \end{array} \right] \left[\begin{array}{c} x_K \\ e \end{array} \right], \quad (23)$$

where the error e consists of $n_e = 11$ entries: lateral position (r_y, r_z), velocities v , angular rates ω and imaginary part of attitude quaternion (q_1, q_2, q_3); and the action u consists of fins δ_{thr} and thrusters δ_{fins} . Note that the reference frame notation is dropped here and all quantities are defined in (13).

The controller order is selected so that, by choosing A_K and C_K diagonal, each state corresponds to a single actuator channel. As for B_K and D_K , the non-zero pattern is selected based on the coupling between actuators and outputs inferred from the dynamic equations (11). This is done in a quantitative manner by inspecting the magnitude of the coefficients in the associated matrices B and D from the linearized model. For example, the x -axis thruster has a strong impact on ω_x , while the first pair of fins has it on ω_y . Table 3 illustrates the non-zero pattern prescribed for B_K and D_K based on this assessment. The initialization of the matrices in (23) is such that $A_K = -I_{7 \times 7}$ and all the other non-zero elements are equal to 1. We also explore the *RandomStart* initialization option provided by *systune* to test multiple optimization runs with different initializations (number of runs set here to 6).

Table 3 Coupling between output (rows) and input (columns) denoted by X and used to determine the non-zero patterns of B_K and D_K .

	$\delta_{\text{thr},x}$	$\delta_{\text{thr},y}$	$\delta_{\text{thr},z}$	$\delta_{\text{fins},1}$	$\delta_{\text{fins},2}$	$\delta_{\text{fins},3}$	$\delta_{\text{fins},4}$
r_y	X			X	X		
r_z		X			X	X	
v_x	X			X	X	X	X
v_y		X			X	X	
v_z	X			X	X		
ω_x	X						
ω_y		X		X	X		
ω_z			X			X	X
q_1	X	X	X	X	X	X	X
q_2	X	X	X	X	X	X	X
q_3	X	X	X	X	X	X	X

Denoting the entries of the two diagonal matrices as $A_K = \text{diag}(a_{ii})$ and $C_K = \text{diag}(c_{ii})$, and the non-zero entries of the other two matrices by b_{ij} and d_{ij} , the transfer function from the error $e = [e_1 \dots e_{n_e}]$ to the i -th action u_i is

$$u_i = \frac{1}{s - a_{ii}} \sum_j^{n_e} (d_{ij}s + (c_{ii}b_{ij} - a_{ii}d_{ij})) e_j. \quad (24)$$

Each actuator thus corresponds to a first-order lead-lag compensator. The overall controller structure is different than the one considered in previous works. Specifically, the lag structure and the MIMO configuration as opposed to a SIMO one where only four gains were optimized are important distinctions with respect to the design proposed in [27] for the VEGA launcher (ascent flight). As opposed to the cascaded control proposed in [13] for the CALLISTO project (descent flight), controller (23) considers in an integrated way both attitude and translational objectives. Another difference with [13] is the use therein of virtual control commands. Whereas they can be advantageous for control design, they might hide the effectiveness of the actuators. By mapping directly the errors to fins and thruster actions as done in (24), capabilities and limitations of the actuators can be determined during the control synthesis process.

2. Gain scheduling

The plant P capturing the RLV dynamics (Figure 7) changes significantly through the flight mission, mainly due to variations associated with the generation of aerodynamic loads. To exemplify this, Figure 8 shows the Bode plots of the thruster and fin to quaternion channels when the model is linearized at the 7 altitude values reported in the legend. Designing a fixed controller which is deployed for all altitudes would inevitably result in performance degradation and lack of robustness.

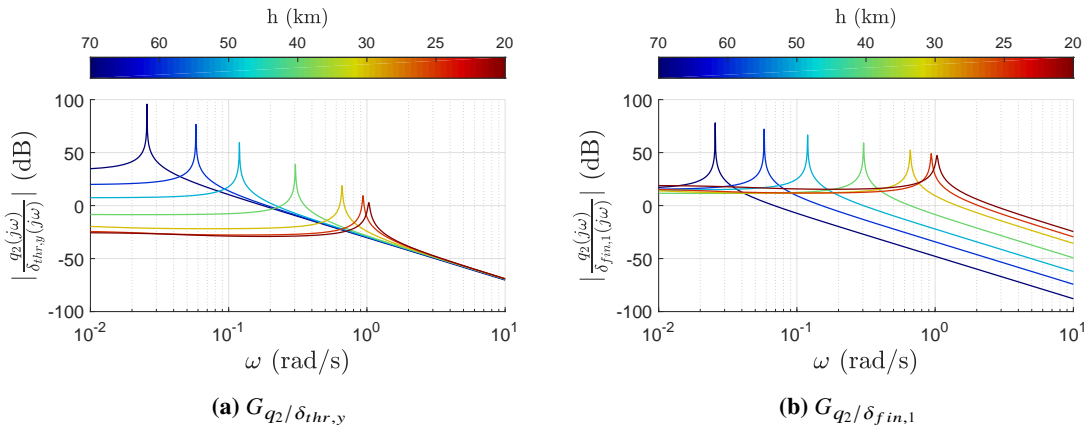


Fig. 8 Quaternion transfer functions with respect to altitude.

The gain-scheduling technique [34] allows these variations to be accounted for by selecting a set of operating points adequately representing the time-varying properties and designing a controller for each one of these points. Precisely, gain-scheduling prescribes the selection of the *scheduling parameter* and the *gain schedule*, i.e. a strategy for implementation and combination of the designed controllers.

The selection of scheduling parameters has been amply studied in space applications. In [35] the authors review different options such as time, non-gravitational velocity, dynamic pressure and altitude. The most desired property of a scheduling parameter for space applications is to be representative of the changing aerodynamics loads. Despite this is the case for dynamic pressure, this is not monotonic with respect to time. For this reason, and following another recent work focused on the descent flight [13], the altitude is selected as scheduling parameter as it is monotonically decreasing and is correlated to the system parameters' evolution.

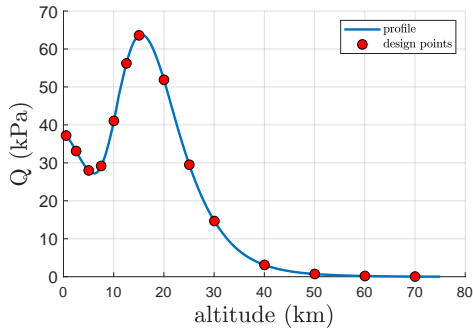


Fig. 9 Dynamic pressure with respect to altitude for the nominal trajectory.

The selection of design points for controller synthesis aims at covering the time-varying system dynamics and, thus, the evolution of dynamic pressure through the mission. In this work, 14 design points are selected and defined in Table 4. As it can be observed from Figure 9, this selection adequately captures the variation in dynamic pressure.

Table 4 Design points with respect to altitude.

Scheduling parameter	Design points														
Altitude (km)	70	60	50	40	30	25	20	15	12.5	10	7.5	5	2.5	0.5	

For each design point $\{h_\lambda\}_{\lambda=1}^N$, a controller is designed based on the model for the corresponding plant P , resulting in a family of linear controllers $\{K_\lambda\}_{\lambda=1}^N$. To smoothly combine this family of discrete controllers, a signal blending scheme is adopted, see Figure 10. It consists of a parallel configuration where the input and output blending coefficients c_i and c_o determine which controller is activated and how the controller signals are interpolated, respectively. The

input signal is the error e from the plant, common for all controllers, while the output signal is the control action u obtained from the interpolation scheme. A qualitatively similar blending signal strategy has already been adopted, e.g. in [36, 37].

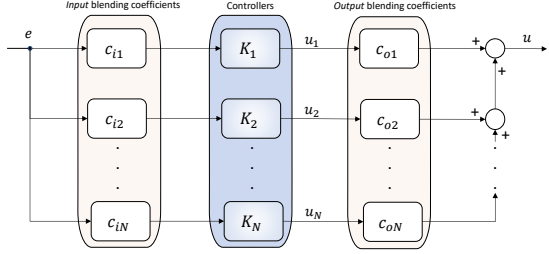


Fig. 10 Controllers blending principles for gain scheduling.

The purpose of the coefficients c_i is to warm-up the controllers so that they have a non-zero initial state when their output is used to control the plant. The output coefficients c_o are used instead to blend the control signals of each controller. To exemplify how the scheduling is implemented, let us consider the transition between K_λ and $K_{\lambda+1}$. Table 5 and Table 6 show the output and input coefficients law, respectively. In the first phase, K_λ is the only active controller on the plant ($c_{o,\lambda} = 1$, $c_{o,\lambda+1} = 0$) and is the only one running on board ($c_{i,\lambda} = 1$, $c_{i,\lambda+1} = 0$). As the scheduling variable gets closer to the new design point, the two set of coefficients change. Considering first the output coefficients, the transition between two controllers starts at $h_{\lambda,o} = h_\lambda + \lambda_o(h_{\lambda+1} - h_\lambda)$, where λ_o is empirically set to 0.85. In this phase, $c_{o,\lambda+1} \in (0, 1]$ and thus the new controller $K_{\lambda+1}$ is activated according to the linear interpolation law defined in Table 5. As for the input coefficients, the corresponding transition altitude is $h_{\lambda,i} = h_\lambda + \lambda_i(h_{\lambda+1} - h_\lambda)$, with $\lambda_i = 0.6 (\leq \lambda_o)$. The controller $K_{\lambda+1}$ is warmed up by setting ($c_{i,\lambda+1} = 1$). Note that, because $\lambda_i < \lambda$, controller $K_{\lambda+1}$ is activated (and thus its state initialized) before its output is applied to the plant. Computing the input thus entails running in parallel at most two controllers at any time.

Table 5 Output blending coefficients.

$c_{o,\lambda}$	$c_{o,\lambda+1}$	Condition
1	0	$h_\lambda \geq h > h_{\lambda,o}$
$\frac{h-h_{\lambda+1}}{h_{\lambda,o}-h_{\lambda+1}}$	$1 - c_{o,\lambda}$	$h_{\lambda,o} \geq h > h_{\lambda+1}$
0	1	$h_{\lambda+1} \geq h \geq h_{\lambda+1,o}$

Table 6 Input blending coefficients.

$c_{i,\lambda}$	$c_{i,\lambda+1}$	Condition
1	0	$h_\lambda \geq h > h_{\lambda,i}$
1	1	$h_{\lambda,i} \geq h > h_{\lambda+1}$
0	1	$h_{\lambda+1} \geq h \geq h_{\lambda+1,i}$

This blending strategy presents one main disadvantage, namely large transients can occur in the switching region due to the fact that the neighbouring controllers are warmed-up by running open-loop before entering in action (i.e. there is no feedback on the effect of the signal u_i in Figure 10 unless this corresponds to the active controller). The main advantage is that the individual controllers are not required to present strong similarities in their structure and/or in the values of the control parameters, allowing for more flexibility. This trade-off should be better investigated in future works, and the implementation of improved scheduling strategies is an important extension to achieve better robustness properties.

C. Generalized plant definition

In order to cast the controller design for RLV as the robust control problem discussed in Section III.B, the generalized plant used for the structured \mathcal{H}_∞ design (22) needs to be defined. The starting point is the block diagram pictorially represented in Figure 11, and consisting of three main dynamic blocks: the linearized system dynamics G_{RLV} discussed in Section II.C, the wind model G_{wind} and the controller K to be designed. A set of weights are also introduced to include design specifications, namely: W_c for references scaling, W_w for wind disturbances, W_u for control signals limitations, W_{qe} for error attitude performance and W_z for outputs tracking performance.

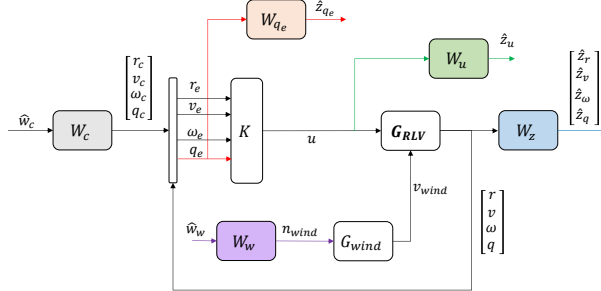


Fig. 11 RLV closed loop diagram.

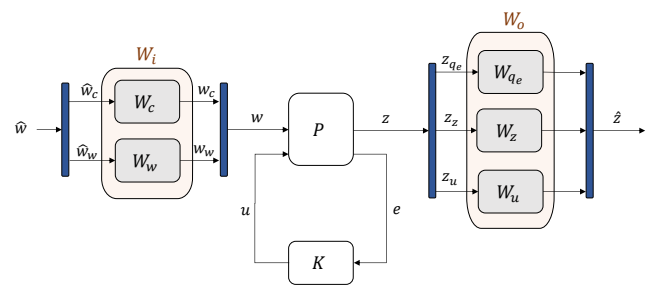


Fig. 12 Weighted \mathcal{H}_∞ configuration.

The interconnection in Figure 11 can then be transformed in the desired generalized plant shown in Figure 12, consisting of the augmented system dynamics P , the controller K and the input W_i and output W_o weights associated with the design specifications. The input signals to the generalized plant include the weighted reference w_c , wind inputs w_w , and control signal u . The output signals include the quaternion error z_{qe} , output variables z_z , control signal z_u , and the error e fed to the controller. The weights W_i and W_o are block diagonal matrices gathering the weight matrices from Figure 11. The next sections will provide details on the characterization of the wind disturbance and selection of the weights.

1. Wind disturbance

Wind gusts can cause important effects on the generation of aerodynamic loads and potentially result in unacceptable performance degradation, especially in low altitude and high air density conditions. Within the adopted robust control framework, wind gusts can be modelled as low-frequency disturbances and taken into account explicitly in the design phase to achieve satisfactory disturbance rejection properties. This is done by defining the block G_{wind} in Figure 11. To this aim, consider a classic wind model according to which the wind velocity v_w is generated by feeding zero-mean, unit-variance Gaussian noise n_w into the Dryden filter G_w . The latter represents an atmospheric turbulence model generating colored wind velocity components as a function of environmental variables [38]

$$G_w(s) = \frac{v_w(s)}{n_w(s)} = \frac{\sqrt{\frac{2}{\pi} \frac{\|v\|_2 - v_h}{L_h} \sigma_h^2}}{s + \frac{\|v\|_2 - v_h}{L_h}}, \quad (25)$$

where v is the launcher velocity, L_h is the turbulence length scale, σ_h is the wind gust standard deviation and v_h is the wind velocity vertical profile. The last three variables can be obtained as a function of the altitude [39]. The low-pass frequency response of the considered Dryden filter is depicted for different altitudes in Figure 13.

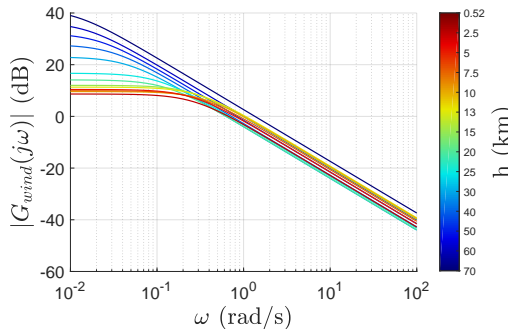


Fig. 13 Bode diagram of the Dryden filter as a function of the altitude.

The wind velocity v_w can be transformed in the wind signal v_{wind} entering the airspeed model (5) by assigning appropriate directions. The vector v_{wind} is assumed to lie on the plane defined by the $Y_L - Z_L$ axes of the LP frame. The

resulting wind disturbance model can be written as

$$L^v_{\text{wind}} = \underbrace{\begin{bmatrix} 0 & 0 \\ G_w & 0 \\ 0 & G_w \end{bmatrix}}_{G_{\text{wind}}} n_{\text{wind}}, \quad (26)$$

where $n_{\text{wind}} = (n_{w1}, n_{w2})$ is a two-dimensional Gaussian noise vector and G_{wind} is the MIMO wind model transfer function to be used in the generalized plant.

2. Weight selection

The selection of the weights in Figure 12 concludes the definition of the generalized plant. This step is done by following the general procedure for \mathcal{H}_{∞} design [31], where the overall goal is to obtain good tracking performance (according to the requirements presented in Table 2) and disturbance rejection by shaping sensitivity and complementary sensitivity functions.

Starting from the input weights, the reference weight matrix W_c is a block diagonal matrix consisting of the blocks W_{r_c} , W_{v_c} , W_{ω_c} , and W_{q_c} representing lateral position, velocity, angular rates and quaternion contributions, respectively. Their values are determined based on the allowed maximum value for the input references of the corresponding channel. For example, we set $W_{q_c} = 0.02I_{3 \times 3}$ in view of a maximum expected quaternion reference of 0.02, selected based on the fact that a quaternion with imaginary part $[0 \ 0.02 \ 0]$ results approximately in a pure rotation of 1° around the corresponding axis. The angular rate weight is also selected equal to $W_{\omega_c} = 0.02I_{3 \times 3}$ using the same rationale. As for the translational channels, the position $W_{r_c} = \text{diag}(W_{r_{yc}}, W_{r_{zc}})$ and velocity $W_{v_c} = \text{diag}(W_{v_{xc}}, W_{v_{yc}}, W_{v_{zc}})$ weights vary in general as a function of the altitude. The following choices are made here: $W_{v_{xc}} = 10$, $W_{v_{yc}} = 1$, $W_{v_{zc}} \in [1, 10]$, $W_{r_{yc}} = 1$ and $W_{r_{zc}} \in [50, 150]$. The disturbance weight W_w scales the random noise vector n_{wind} and was selected as $W_w = f_w \begin{bmatrix} 1 & 0 \\ 0 & 1 \end{bmatrix}$ where $f_w = 3\sigma_{\text{wind}}$ and σ_{wind} is the standard deviation of the noise and determines the variability of wind cases captured in the control design. Based on simulations-based tuning, $f_w \in [0.01, 1.5]$ where the minimum value 0.01 is present only in the design point at $h = 15$ km.

As for the output weights, the main criterion used to select them is based on the accepted performance level for the various channels. The error attitude weight matrix W_{q_e} is a diagonal matrix consisting of the filters associated with the corresponding quaternion channels

$$W_{q_{ie}}^{-1} = 0.02 \frac{h_{q_{ie}} s + \omega_{q_{ie}}}{s + \frac{\omega_{q_{ie}}}{l_{q_{ie}}}}, \quad i = \{1, 2, 3\}$$

where $h_{q_{ie}}$ is the desired peak value of the associated sensitivity function, $l_{q_{ie}}$ is the desired low frequency asymptote, $\omega_{q_{ie}}$ is the desired bandwidth, while 0.02 is used for scaling purposes. The peak is selected in the range $h_{q_{ie}} \in [1.5, 3]$, which corresponds to a gain margin $GM \geq 1.5$ and phase margin $PM \geq 20^\circ$. The peak is chosen close to 3 at high altitudes ($h > 50$ km) where the fins present low effectiveness due to low dynamic pressure while tighter requirements (i.e. peak close to 1.5) are adopted at lower altitudes ($h < 30$ km) since air density is higher, fins can provide more actuation power and higher stability margins are desirable since aerodynamic forces are stronger. Because controlling translational degrees of freedom poses limitations to the low frequency attitude sensitivity [27], it is chosen $l_{q_{ie}} \in [0.75, 0.9]$. The bandwidth is finally set as $\omega_{q_{ie}} \in [0.025, 0.25]$ rad/s.

The output weight matrix W_z is a diagonal matrix consisting of the scalar weights W_r , W_v , W_{ω} and W_q associated with the corresponding output signals already introduced. The quaternion weight W_q shapes the complementary sensitivity function T_{q_i} of each i -th quaternion and is selected as

$$W_{qi}^{-1} = \frac{h_{qi} s + \omega_{qi}}{s + \frac{\omega_{qi}}{l_{qi}}}, \quad i = \{1, 2, 3\}$$

where h_{qi} , l_{qi} and ω_{qi} have the same interpretation as before. Based on the fundamental relationship between sensitivity and complementary sensitivity, W_{qi} is related to the previous attitude performance weight $W_{q_{ie}}$. Hence l_{qi} is set equal

to the desired sensitivity peak, i.e. $l_{qi} = h_{qie}$, as also done in [27]. The tracking bandwidth ω_{qi} is set to 20 rad/sec as a reasonable trade-off between over-constrained specifications and high-frequency attenuation. The high frequency asymptote h_{qi} is fixed to 10^{-3} . For the position $W_r = \text{diag}(W_{ry}, W_{rz})$ and velocity $W_v = \text{diag}(W_{vx}, W_{vy}, W_{vz})$ weights the specifications from [27] are used, since the booster stage is similar to that studied therein. Precisely, the same order of magnitude from [27] is used and a simulation-based tuning is used to refine the exact values. The final result is

$$W_{ry}^{-1} = 20 \quad W_{rz}^{-1} \in [250, 400] \quad W_{vx}^{-1} = 15 \quad W_{vy}^{-1} = 10 \quad W_{vz}^{-1} \in [10, 15].$$

The angular velocity weights W_ω do not impose explicit requirements and are set to

$$W_\omega^{-1} = \text{diag}(1, 1, 1) \text{ rad/s.}$$

The control input weight matrix W_u is used to impose signal limitations and thus prevent from actuator saturation. In aerodynamic descent, the RLV consists of 7 different actuators, namely three thrusters and four fin deflection angles. We design W_u such that the maximum allowable control actions are not violated based on the aforementioned requirements and introduce low pass filters to attenuate high frequency control signals. To this aim, the fin weight is selected as $W_{\text{fin}}^{-1} = \frac{h_{u,\text{fin}}s + \omega_{u,\text{fin}}}{s + \frac{\omega_{u,\text{fin}}}{l_{u,\text{fin}}}}$ where $h_{u,\text{fin}} = \frac{\pi}{180^\circ} 1^\circ$, $l_{u,\text{fin}} \in \frac{\pi}{180^\circ} [13, 20]^\circ$ and $\omega_{u,\text{fin}} = 10 \text{ rad/s}$ represent high, low frequency asymptotes, and actuation bandwidth, respectively. The thrusters weight are instead set to $W_{\text{thr}}^{-1} = 1$. The weight matrix W_u is thus given by

$$W_u = \text{diag}(W_{\text{thr}}, W_{\text{thr}}, W_{\text{thr}}, W_{\text{fin}}, W_{\text{fin}}, W_{\text{fin}}, W_{\text{fin}}).$$

IV. Robustness in the face of trajectories: a multi-plant design approach

The control design procedure described in Section III relies on the perfect knowledge of the trajectory to be tracked during the descent phase. This is indeed leveraged to obtain the linearized models used for the design of the scheduled structured \mathcal{H}_∞ controllers. As discussed earlier, knowledge of the optimal trajectory is often not available in the offline design phase due to the uncertainty on the plant, the environment, and its time-varying properties. One approach to overcome this is to use a closed loop guidance algorithm, which is capable of updating the optimal reference signal online. However, this can cause robustness issues in the (offline) designed robust controller unless the reference trajectory variability has been already accounted for. This Section provides a strategy to address this robustness issue by a two-step procedure: first, a tube of trajectories covering possible references generating online by the guidance algorithm is computed; second, a controller which is robust to the range of plants associated with the tube is synthesized.

A. Tube of trajectories emulating closed loop guidance

The construction of the tube of trajectories builds on the methodology proposed in Section II.D.2 to generate a family of reference trajectories by sampling different initial velocity conditions. These trajectories form a tube around the nominal trajectory. Specifically, the tube is bounded by two extreme trajectories, namely an *upper* trajectory associated with initial velocity $(_L v_y(t_0), _L v_z(t_0)) = (200, 1500) \text{ m/s}$ and a *lower* trajectory associated with initial velocity $(_L v_y(t_0), _L v_z(t_0)) = (-75, 800) \text{ m/s}$. The other trajectories are generated by considering dispersion ranges $\{-200, 200\} \text{ m/s}$ for the initial crossrange velocity and $\{800, 1500\} \text{ m/s}$ for the initial downrange velocity. Figure 14 illustrates the tube where upper, lower and nominal (center) trajectories are shown with black lines, while other tube trajectories are depicted with cyan dashed lines. For the sake of clarity, the trajectories are shown in XZ plane but they also contain components in the crossrange direction. Red markers indicate the design points.

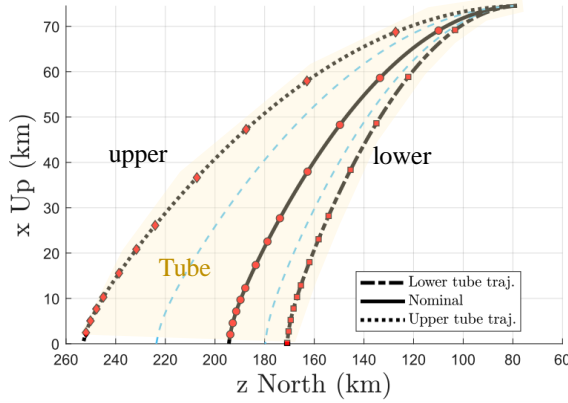


Fig. 14 Tube of trajectories.

This tube generation procedure is of course only one possible option and could be modified to leverage some problem-specific information, e.g. parameterizing the off-nominal trajectories that are expected to be generated by the guidance algorithm. This is an interesting research question left for future work.

The linearized plants associated with the trajectories in the tube show different dynamical properties even when compared at the same altitude. This can be observed in Figure 15, which shows the different dynamic pressure profiles of upper, lower and nominal reference trajectories as a function of the altitude. The differences are more marked in the region between 15 and 40 km due to importance of the aerodynamic loads. The different properties associated with the variability in the trajectories are also visible in Figure 16, which displays the open-loop magnitude Bode plots of the downrange position channel for two design points at 20 and 25 km.

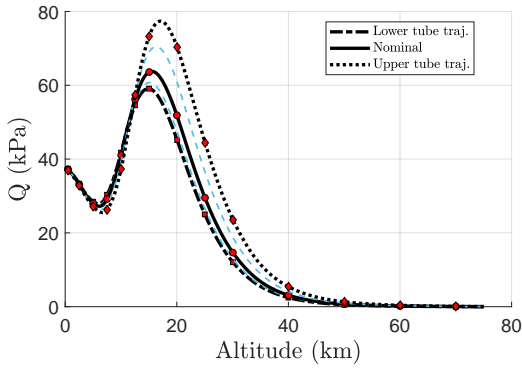


Fig. 15 Dynamic pressure profiles.

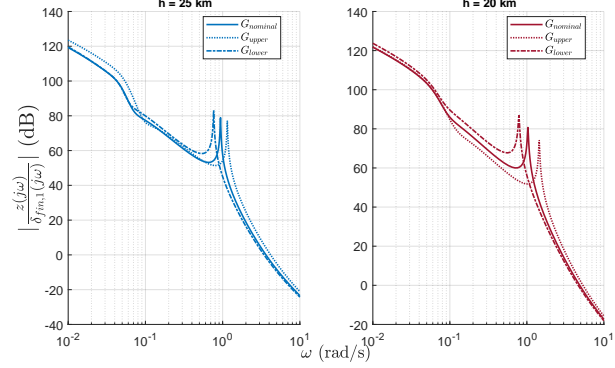


Fig. 16 $G_{z/\delta_{fin,1}}$ at $h=20\text{km}$ and $h=25\text{km}$.

Variability of nominal, upper and lower models.

B. Multi-plant control design

In view of the observed dispersion of dynamical properties caused by the uncertainty on the reference trajectories, the goal is to provide a gain-scheduled (and designed offline) controller which satisfies system specifications for a set of models (defined by the tube of reference trajectories) at each design point, instead of the nominal one as typically done. To this aim, the structured \mathcal{H}_∞ synthesis approach discussed in Section III.B is augmented with a multi-plant design strategy. In particular, models obtained by upper, lower and nominal trajectories will be used for control synthesis, on the premise that these trajectories are representative of the variability.

As investigated numerically in Section V, this choice will bring about a trade-off between performance and robustness. The nominal design maximizes the performance of the assumed known trajectory but ignores degradations potentially

occurring due to the actual (unaccounted for) conditions. On the other hand, the multi-plant prioritizes robustness against all the trajectories captured by the three chosen candidates at the price of a degradation of (nominal) performance.

The multi-plant \mathcal{H}_∞ problem can be formulated as the multi-objective optimization problem

$$\begin{aligned} \min_K & \max_{\substack{j=1 \\ \text{upper,} \\ \text{nominal,} \\ \text{lower}}} \left(\left\| W_o T_{wz}^j W_i \right\|_\infty \right), \\ \text{s.t.} & K \text{ stabilizes } P_{\text{upper}}, P_{\text{nominal}}, P_{\text{lower}} \text{ internally,} \\ & K \in \mathcal{K}_{\text{struct}}, \end{aligned} \quad (27)$$

where upper, nominal and lower superscripts/subscripts refer to models derived by the upper, nominal and lower reference trajectories, respectively. That is, the problem is posed as the search for the controller minimizing the worst-case (weighted) \mathcal{H}_∞ norm among the three generalized closed loop functions. Problem 27 is solved through the *systune* routine of MATLAB, which provides automatic tuning of fixed-order controllers with respect to multiple models based on the approach from [40]. The multi-plant design approach does not guarantee performance satisfaction for all the plants associated with trajectories in the tube, but it proved successful in extensive simulation campaigns, as shown in Section V. An alternative approach which comes with stronger theoretical guarantees is by means of μ synthesis [30], which is left for future research.

V. Simulation results

This Section shows numerical results to demonstrate the validity of the synthesis approaches presented in the paper. The closed-loop behavior is analyzed both with classic frequency-domain linear tools and with nonlinear time-domain simulations conducted using the nonlinear RLV model described in Section II. The focus of the work is on the aerodynamic part of the descent flight where the actuators are aerodynamic fins and thrusters. The analyses however consider the descent phase up to landing in order to explore the capabilities of fins and thrusters at low altitudes, in consideration of the fact that in the lower altitude region aerodynamic loads and wind gusts are stronger and thus the effectiveness of fins and thrusters can become critical. This investigation is also useful as a preliminary analysis for determining variability in the starting condition of powered descent. The codes implementing these tests are freely accessible from the supplemental material of [25].

A. Nominal trajectory controllers

Figure 17 shows the complementary sensitivity functions T and reference weights for a set of input-output channels (namely outputs q_2, z, v_z and wind inputs n_{wy}, n_{wz}). The weights W_{out} are obtained by multiplying the appropriate output and input weights, e.g. for the channel z/v_{zc} the relative weight is $W_{\text{out}} = W_{rz} W_{v_{zc}}$, where W_{rz} and $W_{v_{zc}}$ were defined in Section III.C.2. Only the design point at $h = 5$ km, which corresponds to one of the highest dynamic pressure, is depicted. It can be observed that in all cases the transfer functions satisfy the requirements prescribed through the frequency weighting.

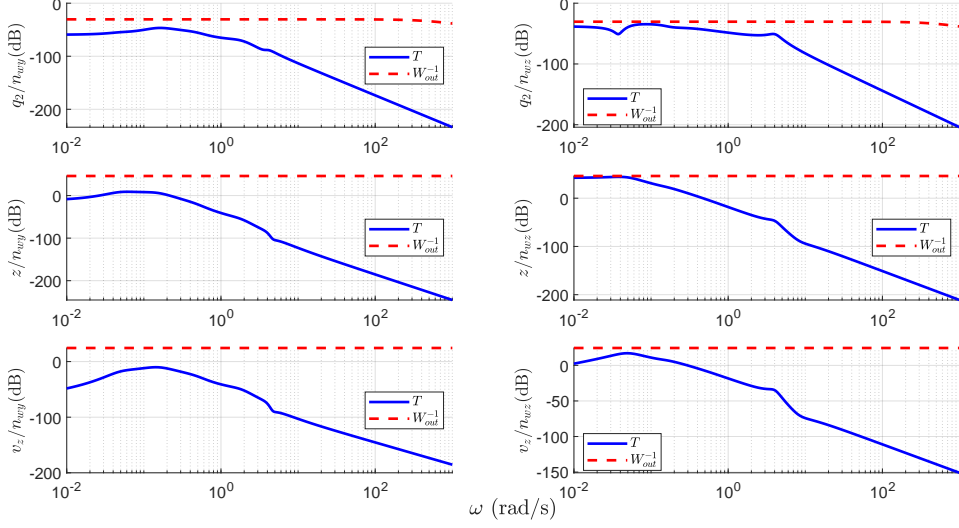


Fig. 17 Bode plots from wind to controlled output channels at $h = 5 \text{ km}$.

The gain scheduled controllers are then evaluated in time-domain simulations where the goal is to track the nominal reference trajectory despite the presence of wind gusts. A Monte Carlo campaign with 200 wind profiles generated by coloring white noise through Dryden filters is studied. The performance is compared with that of a nominal \mathcal{H}_∞ controller designed without the disturbance rejection requirements (i.e. with no \hat{w}_w channel in the generalized plant in Figure 12).

It is recalled that the control objective here is to achieve a load relief strategy whereby the wind-induced aerodynamic loads are reduced. To do so, the vehicle will have to drift from the prescribed translational reference, and by doing so improve on the attitude tracking to keep the angle of attack close to 180° . The arising trade-off between attitude error-minimum, drift-minimum and load-minimum strategies is thoroughly explained in [27]. If the goal was instead to minimize the translational errors, a higher value for the weight W_w should have been selected (see Section III.C).

Figure 18 shows the pitch errors for the simulated scenarios. Each individual Monte Carlo run is depicted with light transparent color, whereas the mean error is represented by a bold line. It is apparent that the controller designed for wind rejection purposes achieves lower error values (and thus lower deviation from the expected loads), especially in the low altitude range.

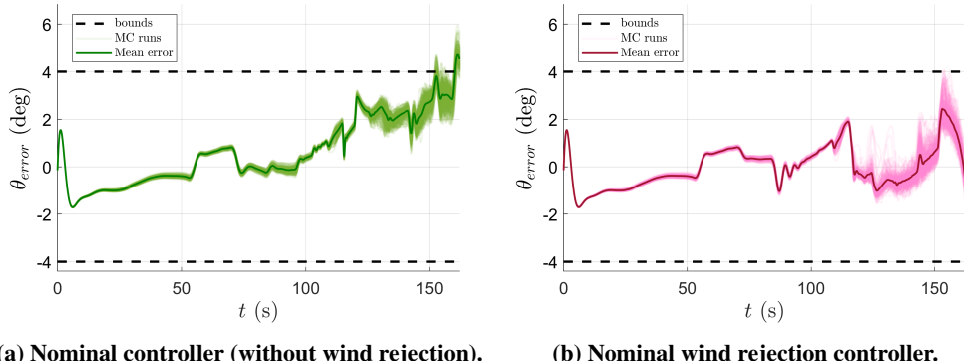
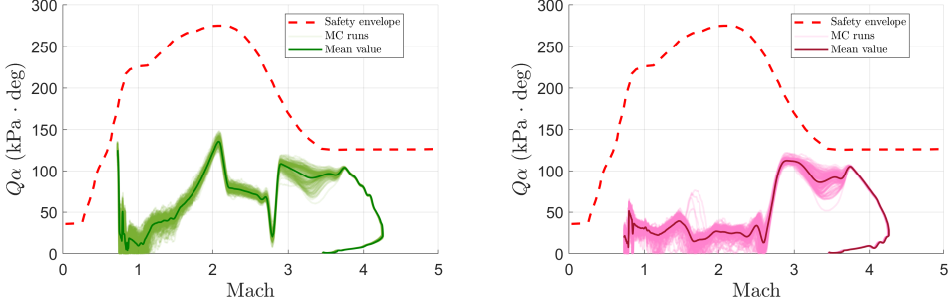


Fig. 18 Pitch θ error profiles.

Figure 19 illustrates the $Q\alpha$ profiles. The proposed controller is confirmed to obtain a better load relief as most of the profile values are below 50 kPa deg in the region $\text{Mach} \leq 2.5$, where the wind presents the highest impact.

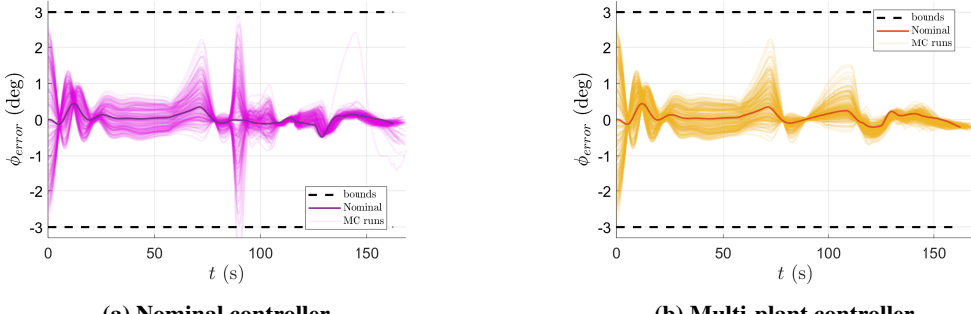


(a) Nominal controller (without wind rejection). **(b) Nominal wind rejection controller.**

Fig. 19 $Q - \alpha$ profiles (safety envelopes from [27]).

B. Multi-plant trajectory controllers

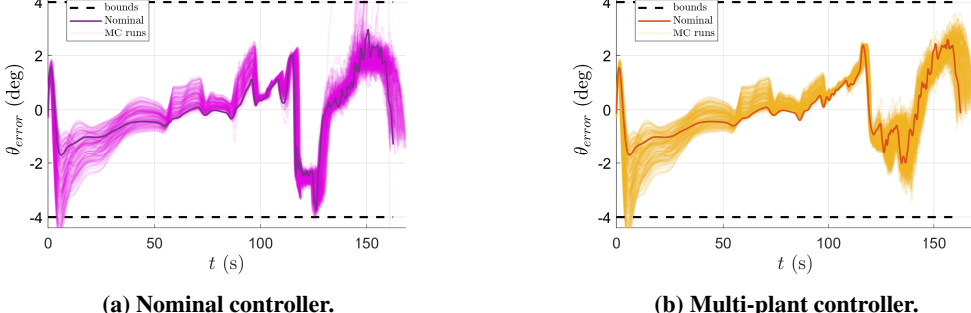
The (linear) frequency-domain analysis at single design points are aligned with what was observed in the previous section, therefore the focus is here on (nonlinear) time-domain simulations. The 200 reference trajectories used for Monte Carlo analysis, are generated by uniformly sampling different initial lateral velocities in the range [-100, 100] m/s for crossrange direction and [800, 1500] m/s for downrange direction. Wind disturbances are also introduced similarly to what discussed in the previous section. The multi-plant controller (orange) is compared against the nominal controller (purple). The response corresponding to the nominal trajectory is denoted with a bold line. Figures 20 - 24 show overall a significant improvement with the multi-plant controller. Indeed, while this leads to smoother error profiles and respects all the performance specification, in some of the runs the nominal controller showed error responses violating the bounds and even diverging sharply.



(a) Nominal controller.

(b) Multi-plant controller.

Fig. 20 Roll ϕ error profiles.



(a) Nominal controller.

(b) Multi-plant controller.

Fig. 21 Pitch θ error profiles.

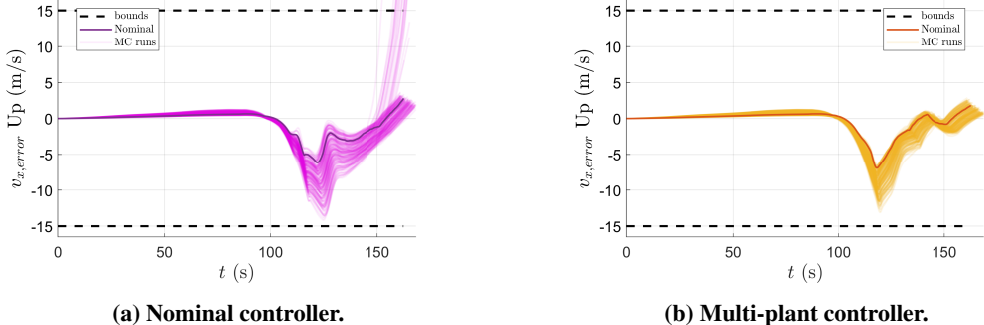


Fig. 22 Altitude velocity v_x error profiles.

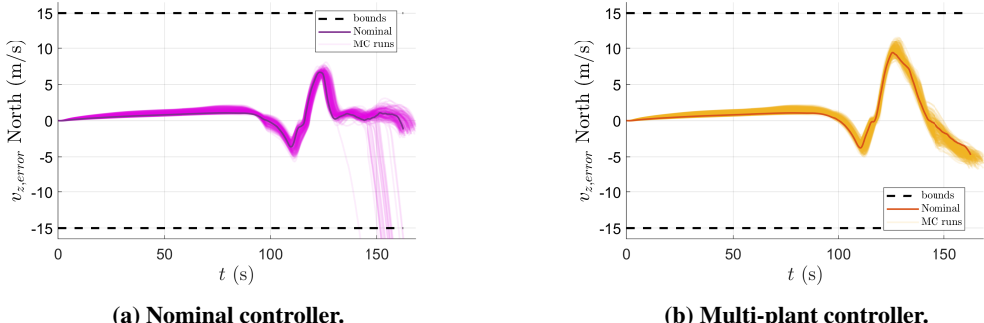


Fig. 23 Downrange velocity v_z error profiles.

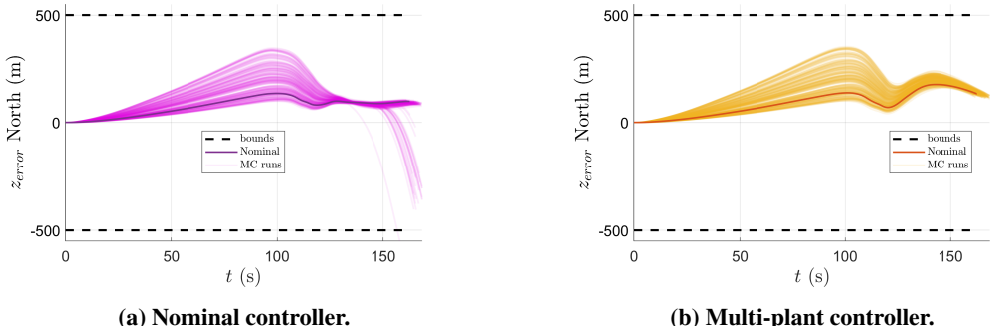


Fig. 24 Downrange z error profiles.

To further quantitatively compare the nominal and multi-plant controllers, so-called spider charts are generated. These are computed by considering ∞ -norm (i.e. absolute maximum value) and 2-norm (i.e. signal energy) metrics for position, velocity, and attitude errors signals, as well as for thrusters and fins actuation. These metrics are calculated for each Monte Carlo run, and their values are averaged. The average multi-plant metrics are then normalized by the corresponding average nominal tuning metrics in order to make a direct comparison between the controllers. That is, the multi-plant controller achieves better performance in a certain metric whenever the corresponding chart is inside the dashed black chart.

Figure 25a depicts the spider chart for the error state metrics. It can be appreciated that the multi-plant wind-rejection controller outperforms the nominal one in the majority of metrics. Figure 25b shows the actuators spider charts. It can be noted here that the first fin $\delta_{fin,1}$ and thruster $\delta_{thr,y}$ metrics are higher for the multi-plant approach. This can be

interpreted from the fact that more actuation effort might be needed to attenuate the impact of wind disturbances and to mitigate the wind-induced drifts.

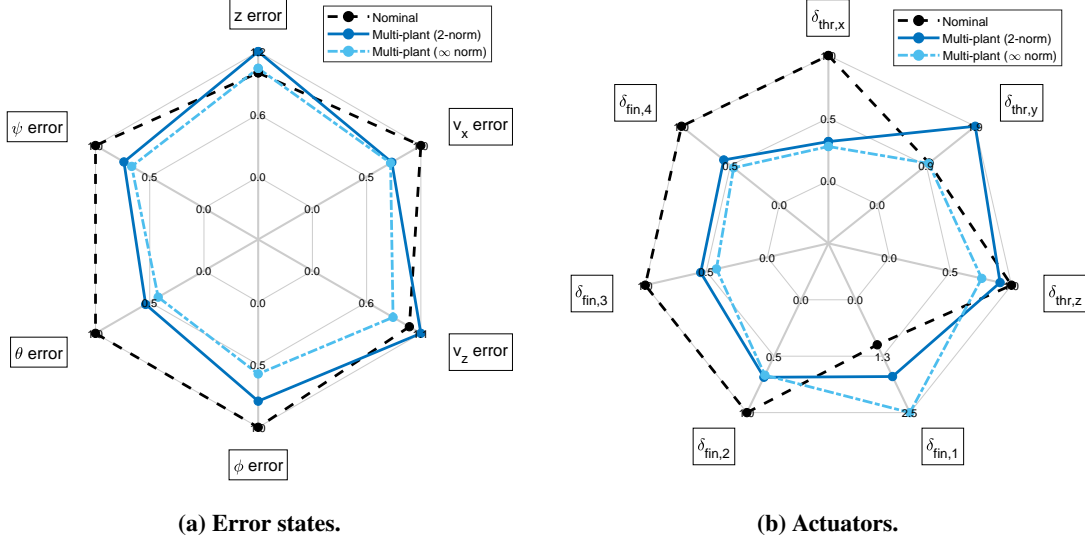


Fig. 25 Spider charts for nominal and multi-plant controllers on tube trajectories.

A final analysis is conducted in order to investigate the performance vs. robustness trade-off associated with the multi-plant design. To this aim, the two controllers (nominal and multi-plant) are evaluated in the scenario where they need to track the nominal reference trajectory in the presence of wind gusts (the usual Monte Carlo analysis based on generating 200 different wind profiles is considered). Figure 26 depicts the error state spider chart. The nominal controller outperforms the multi-plant in downrange position and velocity. Furthermore, the multi-plant controller presents now worse performance for roll, yaw and altitude velocity metrics compared to the one it showed in Figure 25a for off-nominal conditions. In general, nominal and multi-plant metrics are closer than in the off-nominal scenario, revealing a performance loss of the multi-plant controller in nominal conditions. However, its performance remains for most of the metrics superior to the nominal one, showing that the proposed design leads to an overall satisfactory point in the known trade-off curve between performance and robustness.

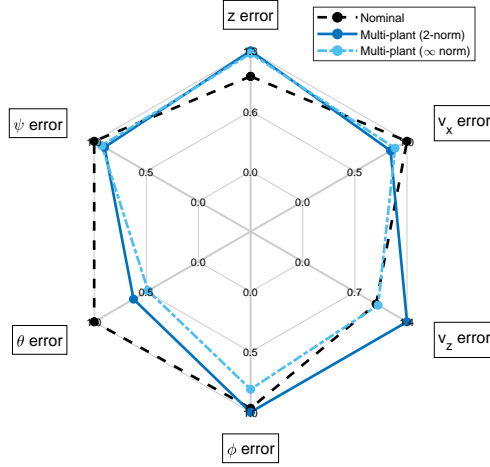


Fig. 26 Spider charts for nominal and multi-plant controllers on the nominal trajectory (error states).

VI. Conclusion

The paper describes a robust control synthesis approach for the aerodynamic descent phase of reusable launchers. Specific focus is placed on ensuring robustness by design towards the deployment of flexible guidance algorithms. The baseline design includes a gain-scheduled structured \mathcal{H}_∞ controller with reference tracking (for a nominal trajectory) and load relief achieved through disturbance rejection objectives. To emulate the effect of a closed loop guidance algorithm, a tube with candidate reference trajectories is defined and robustness is provided via multi-plant \mathcal{H}_∞ design. The results show good performance of the baseline controller when tracking the nominal reference subject to wind disturbance. Moreover, the multi-plant approach leads to a considerable improvement on the robust performance for off-nominal scenarios compared to the baseline one without overly sacrificing performance. Future extensions should consider a tightly coupled scenario where the flexibility of the guidance algorithm and the robustness of the controllers are taken into account together in the design. Moreover, improved scheduling strategies such as those offered by the Linear-Parameter-Varying framework could be integrated with the current synthesis framework.

Acknowledgments

This work is partially supported by the Swiss National Science Foundation under grant no. 200021_178890. We acknowledge Embotech AG for helpful discussions on the topic of guidance algorithms for reusable launchers.

References

- [1] Blackmore, L., "Autonomous precision landing of space rockets," *National Academy of Engineering 'The Bridge on Frontiers of Engineering'*, 2016.
- [2] Frosch, J. A., and Vallely, D. P., "Saturn AS-501/S-IC Flight Control System Design," *Journal of Spacecraft and Rockets*, Vol. 4, No. 8, 1967, pp. 1003–1009.
- [3] Edinger, L., "The Space Shuttle Ascent Flight Control System," *Guidance and Control Conference*, 1976, p. 1942.
- [4] Jang, J., Alaniz, A., Hall, R., Bedrossian, N., Hall, C., Ryan, S., and Jackson, M., "Ares I Flight Control System Design," *AIAA Guidance, Navigation, and Control Conference*, 2010, p. 8442.
- [5] Klotz, H., "Ariane 5 Dynamics and Control," *Automatic Control in Aerospace 1992*, Elsevier, 1993, pp. 227–233.
- [6] Doyle, J. C., "Guaranteed Margins for LQG Regulators," *IEEE Transactions on automatic Control*, Vol. 23, No. 4, 1978, pp. 756–757.
- [7] Zames, G., "Feedback and Optimal Sensitivity: Model Reference Transformations, Multiplicative Seminorms and Approximate Inverses," *IEEE Transactions on automatic control*, Vol. 26, No. 2, 1981, pp. 301–320.
- [8] Smith, R., and Ahmed, A., "Robust parametrically varying attitude controller designs for the X-33 vehicle," *AIAA Guidance, Navigation, and Control Conference and Exhibit*, 2000.
- [9] Apkarian, P., and Noll, D., "Nonsmooth H_∞ Synthesis," *IEEE Transactions on Automatic Control*, Vol. 51, No. 1, 2006, pp. 71–86.
- [10] Knoblauch, M., Saussié, D., and Bérard, C., "Structured H_∞ Control for a Launch Vehicle," *2012 American Control Conference (ACC)*, IEEE, 2012, pp. 967–972.
- [11] Navarro-Tapia, D., Marcos, A., Simplício, P., Bennani, S., and Roux, C., "Legacy Recovery and Robust Augmentation Structured Design for the VEGA Launcher," *International Journal of Robust and Nonlinear Control*, Vol. 29, No. 11, 2019, pp. 3363–3388.
- [12] Simplício, P., Marcos, A., and Bennani, S., "Reusable Launchers: Development of a Coupled Flight Mechanics, Guidance and Control Benchmark," *Journal of Spacecraft and Rockets*, Vol. 57, No. 1, 2020, pp. 74–89.
- [13] Sagliano, M., Tsukamoto, T., Heidecker, A., Maces Hernandez, J. A., Fari, S., Schlotterer, M., Woicke, S., Seelbinder, D., Ishimoto, S., and Dumont, E., "Robust Control for Reusable Rockets via Structured H_∞ Synthesis," *11th International ESA Conference on GNC Systems*, 2021.
- [14] Simplício, P., Marcos, A., Joffre, E., Zamaro, M., and Silva, N., "Synthesis and Analysis of Robust Control Compensators for Space Descent & Landing," *International Journal of Robust and Nonlinear Control*, Vol. 28, No. 13, 2018, pp. 3871–3892.

- [15] Sagliano, M., Tsukamoto, T., Maces H., J. A., Seelbinder, D., Ishimoto, S., and Dumont, E., “Guidance and Control Strategy for the CALLISTO Flight Experiment,” *8th European Conference for Aeronautics and Space Sciences*, 2019.
- [16] Greensite, A. L., *Analysis and Design of Space Vehicle Flight Control Systems. Volume II- Trajectory Equations*, Spartan, 1967.
- [17] Isakowitz, S. J., *International Reference Guide to Space Launch Systems*, AIAA, 1991.
- [18] Wie, B., *Space Vehicle Dynamics and Control*, AIAA, 1998.
- [19] Crassidis, J. L., and Junkins, J. L., *Optimal Estimation of Dynamic Systems*, CRC Press, 2004.
- [20] Wie, B., and Barba, P. M., “Quaternion Feedback for Spacecraft Large Angle Maneuvers,” *Journal of Guidance, Control, and Dynamics*, Vol. 8, No. 3, 1985, pp. 360–365.
- [21] Popowski, S., and Dąbrowski, W., “Measurement and Estimation of the Angle of Attack and the Angle of Sideslip,” *Aviation*, 2015.
- [22] Pavlis, N. K., Holmes, S. A., Kenyon, S. C., and Factor, J. K., “The Development and Evaluation of the Earth Gravitational Model 2008 (EGM2008),” *Journal of Geophysical Research: Solid Earth*, 2012.
- [23] “U.S. Standard Atmosphere,” Tech. rep., U.S. Government Printing Office, Washington, D.C., 1976.
- [24] Du, W., “Dynamic Modeling and Ascent Flight Control of Ares-I Crew Launch Vehicle,” Ph.D. thesis, Iowa State University, 2010.
- [25] Gkouletsos, D., “Robust control design towards flexible guidance for reusable space-launch vehicles,” Master’s thesis, ETH Zurich, 2022. <https://doi.org/10.3929/ethz-b-000546276>.
- [26] Simplicio, P. V. M., “Guidance and Control Elements for Improved Access to Space: from Planetary Landers to Reusable Launchers,” Ph.D. thesis, University of Bristol, 2019.
- [27] Navarro-Tapia, D., “Robust and Adaptive TVC Control Design Approaches for the VEGA Launcher,” Ph.D. thesis, University of Bristol, 2019.
- [28] Balas, G., and Packard, A., “Design of robust, time-varying controllers for missile autopilots,” *[Proceedings 1992] The First IEEE Conference on Control Applications*, 1992.
- [29] Apkarian, P., Gahinet, P., and Bannic, J.-M., “Self-scheduled H_∞ control of a missile via LMIs,” *Proceedings of 1994 33rd IEEE Conference on Decision and Control*, 1994.
- [30] Zhou, K., Doyle, J. C., and Glover, K., *Robust and Optimal Control*, Prentice-Hall, Inc., 1996.
- [31] Skogestad, S., and Postlethwaite, I., *Multivariable Feedback Control: Analysis and Design*, Citeseer, 2007.
- [32] Doyle, J., Glover, K., Khargonekar, P., and Francis, B., “State-space solutions to standard H_2 and H_∞ control problems,” *IEEE Transactions on Automatic Control*, Vol. 34, No. 8, 1989, pp. 831–847.
- [33] Gahinet, P., and Apkarian, P., “A Linear Matrix Inequality Approach to H_∞ Control,” *International Journal of Robust and Nonlinear Control*, Vol. 4, No. 4, 1994, pp. 421–448.
- [34] Rugh, W. J., and Shamma, J. S., “Research on Gain Scheduling,” *Automatica*, Vol. 36, No. 10, 2000, pp. 1401–1425.
- [35] Roux, C., and Cruciani, I., “Scheduling Schemes and Control Law Robustness in Atmospheric Flight of VEGA Launcher,” *Proceedings of the 7th ESA International Conference on Spacecraft Guidance, Navigation and Control Systems*, 2008, pp. 1–5.
- [36] Kelly, J., and Evers, J., “An Interpolation Strategy for Scheduling Dynamic Compensators,” *Guidance, Navigation, and Control Conference*, 1997, p. 3764.
- [37] Pusch, M., and Ossmann, D., “ H_2 -Optimal Blending of Inputs and Outputs for Modal Control,” *IEEE Transactions on Control Systems Technology*, Vol. 28, No. 6, 2019, pp. 2744–2751.
- [38] Simplicio, P., Bennani, S., Marcos, A., Roux, C., and Lefort, X., “Structured Singular-Value Analysis of the VEGA Launcher in Atmospheric Flight,” *Journal of Guidance, Control, and Dynamics*, Vol. 39, No. 6, 2016, pp. 1342–1355.
- [39] Johnson, D. L., “Terrestrial Environment (Climatic) Criteria Guidelines for Use in Aerospace Vehicle Development,” *NASA Technical Memorandum, NASA TM 4511*, 1993.
- [40] Apkarian, P., and Noll, D., “Nonsmooth Optimization for Multidisk H_∞ Synthesis,” *European Journal of Control*, Vol. 12, No. 3, 2006, pp. 229–244.